RSC Sustainability

ROYAL SOCIETY OF CHEMISTRY

PAPER

View Article Online
View Journal | View Issue

Cite this: *RSC Sustainability*, 2025, **3**, 3109

Semi-continuous, industrial-like production of transparent cellulose films by means of the Lyocell-type Ioncell® process†

Eva González Carmona, [a] Inge Schlapp-Hackl, [a] Kaarlo Nieminen,[a] Wenwen Fang, [ab] Seppo Jääskeläinen,[c] Kalle Salonen,[d] Hannes Elmer,[e] Helena Westerback, [a] Herbert Sixta [a] and Michael Hummel *[a]

Received 14th February 2025
Accepted 24th May 2025

DOI: 10.1039/d5su00102a

rsc.li/rscsus

A semi-continuous and industrial-like process to produce regenerated cellulose films, based on the Ioncell® technology, is demonstrated. The demand for commercial films, mainly fossil-based, is immense and expected to triple by 2060. This overconsumption leads to drawbacks like fossil reserves depletion and environmental pollution. Therefore, finding sustainable alternative processes compatible with existing industrial operations to produce films from renewable materials like cellulose is crucial. The films herein presented are generated by extruding a cellulose–ionic liquid solution through a distribution plate (DP) and slit nozzle into an aqueous coagulation bath, *via* an air gap. This study evaluates how different DPs and slit geometries affect the extrusion process and the film properties. Moreover, an automated continuous washing and drying system has been successfully implemented. The produced films are thin (13–17 μm), homogeneous, highly transparent (89–91%) and strong. The use of DPs resulted in very strong films (242 MPa, 10% elongation at break) but led to extrusion instabilities. Trials without any DP were stable, with films showcasing tensile strengths of 226 MPa and 9% elongation at break. Additionally, a numerical simulation was performed to understand the effects of the DPs and spinnerets' geometry on the dope flow.

Sustainability spotlight

Developing sustainable processes to produce biodegradable films from renewable materials, as an alternative to commercial synthetic films, is crucial. This will reduce the dependence on petrochemicals and the environmental impact, such as carbon footprint and microplastic pollution. In the presented work, we demonstrate a semi-continuous process that is compatible with existing industrial operations to produce high-quality pure cellulose films. These films are thin, homogeneous, highly transparent, and strong, showing great potential for applications such as packaging, membranes, and battery separators at industrial scale. Our work aligns primarily with the UN Sustainable Development Goal Responsible Consumption and Production (SDG 12) and also addresses Industry, Innovation, and Infrastructure (SDG 9) and Climate Action (SDG 13).

Introduction

In 2019, the global plastic production reached 460 Mt, with only 9% of it being recycled.[1,2] As a result, most plastics were landfilled (50%), incinerated (19%), or even mismanaged (22%). 22 Mt of waste leaked into the environment, including 6 Mt into aquatic environments.[2] With time, these plastics disintegrate into microplastics, which pose great threats to ecosystems, animals, and human health.[3,4] The plastic consumption is expected to nearly triple to *ca.* 1230 Mt by 2060, yet the recycling rate would only reach 17%.[2] In Europe, 54 Mt of plastics were produced in 2023, of which 19.2% were recycled.[5] Despite a higher recycling rate compared to the global average, the amount of waste is still immense, and mainly accounts for single-use-plastic (SUP). To address this pressing issue and promote the development of eco-friendly alternatives from renewable materials, such as cellulose, the European Commission issued the SUP Directive in July 2021, prohibiting or restricting certain SUP products if sustainable substitutes are available.[6] Regenerated cellulose fibres and films produced with the viscose and Lyocell processes were not considered as plastics and are, thus, not affected by the Directive.[7]

[a]*Department of Bioproducts and Biosystems, School of Chemical Engineering, Aalto University, 02150 Espoo, Finland. E-mail: michael.hummel@aalto.fi*
[b]*Campus Straubing for Biotechnology and Sustainability, Technical University of Munich, 94315 Straubing, Germany*
[c]*School of Chemical Engineering, Aalto University, 02150 Espoo, Finland*
[d]*eLabs Oy Engineering, 26100 Rauma, Finland*
[e]*Elmer Gesellschaft m.b.H, 3200 Ober-Grafendorf, Austria*

† Electronic supplementary information (ESI) available. See DOI: https://doi.org/10.1039/d5su00102a

Cellulosic films have been commercially available since 1924, under the tradename Cellophane.[8] Although it was widely displaced by polyolefin films in the 1980s, Cellophane kept a small market share as packaging, tapes and battery separators, among others.[9–11] Despite being considered more sustainable than synthetic films due to the natural origin and renewability of cellulose, the production is based on the viscose process, where the cellulose is treated with carbon disulfide to produce cellulose xanthate, an intermediate derivative that is soluble in caustic soda. Carbon disulphide and sulphurous byproducts present a risk for the environment and human health.[12–15] Therefore, sustainable and eco-friendly alternatives for the production of cellulosic films are needed.

Intensive research has been carried out to develop new systems to generate cellulose films *via* direct dissolution of cellulose. Thin and transparent films have been produced using various solvents, such as lithium chloride/*N*,*N*-dimethylacetamide (LiCl/DMAc),[16–18] tetrabutylphosphonium hydroxide (TBPH),[19] dimethyl sulfoxide/tetrabutylammonium hydroxide (DMSO/TBAH),[20] sodium hydroxide/urea solutions (NaOH/$CO(NH_2)_2$),[17,21,22] and *N*-methylmorpholine *N*-oxide monohydrate (NMMO·H_2O).[10,23–25] Imidazolium-based ionic liquids (IL), *e.g.*, 1-allyl-3-methylimidazolium chloride [amim][Cl], 1-ethyl-3-methylimidazolium chloride [emim][Cl] and 1-ethyl-3-methylimidazolium acetate [emim][OAc], among others, have been also investigated.[26–29] However, most of these solvents systems pose severe challenges for up-scaling because efficient solvent recycling strategies are costly or lacking. NMMO is the only direct cellulose solvent that is recycled on a larger industrial scale. Yet, films produced *via* the NMMO-based Lyocell process are not commercially available.[10,23,24]

In our previous study, a continuous process for the production of cellulose films based on the Ioncell® technology was successfully established.[30] This Lyocell-type process was initially developed by researchers at the University of Helsinki and Aalto University for the generation of high-quality man-made fibres using superbase-based ILs as cellulose solvent.[31] The process is based on 1,5-diazabicyclo[4.3.0]non-5-enium acetate ([DBNH][OAc]), a non-derivatizing cellulose solvent that allows both dissolution and spinning at lower temperatures compared to the NMMO-based process, significantly reducing cellulose degradation.[31–33] Earlier studies have indicated good recyclability of this and related solvents.[34–36] It was shown that by adjusting different parameters of the continuous dry-jet wet spinning process, such as extrusion and take-up velocity, air gap distance, coagulation bath temperature, cellulose concentration and spinning temperatures, thin and transparent films could be obtained. Particularly, films with thicknesses between 12 and 21 μm could reach tensile strengths up to 210 MPa in longitudinal direction, in comparison to 125 MPa found for commercial cellophane.[11,30] Moreover, as the cellulose remains unmodified during the process, the obtained films are exempted from the SUP Directive.[7]

The consequent next step was to investigate the effect of the spinneret geometry on the properties of the generated cellulose films. It is known that different shapes, aspect ratios, entrance cones and diameter holes of the spin capillaries affect the spinnability and fibre properties for the final man-made cellulosic fibres. For instance, Michud *et al.* explored the impact of the hole diameters on the fibre tenacity in the Ioncell® process: higher diameters (200 μm) generated fibres with lower tenacities than smaller diameters (100–150 μm).[37] Hauru *et al.* demonstrated that bigger aspect ratios (L/D) of the spin capillary increased the fibre orientation compared to shorter L/D.[38] More recently, Moriam *et al.* reported that the fibre toughness (up to 83.3 MPa) was improved by increasing the capillary length.[39] Besides, the entrance cone and the shape of the spinneret (circular and rectangular) were tested, resulting in fibres with even higher toughness (93 MPa) when a small entrance angle (8°) and rectangular-shaped spinneret were in use.[40] Mathematical simulations were conducted along these two studies to have a better understanding of the impact of the geometry on the flow of the cellulose solutions inside the spinneret.[39,40]

In this study, we continue the development of the process for the production of cellulose-based films *via* dry-jet wet spinning. The effect of the spinneret geometries on the mechanical properties and morphology of the obtained films was investigated, and the behaviour of the cellulose solutions inside the spinnerets was simulated with computational models. In particular, the slit dimensions, entrance cones of 4, 8 and 13°, and the effect of different distribution plates on the flow behaviour were investigated. Additionally, an automated continuous washing and drying line was successfully implemented. Herein we present high-quality cellulosic films generated by means of a sustainable and semi-continuous process with strong potential for industrial scale-up, as an alternative to commercially available films.

Experimental

Materials

Birch pre-hydrolysis kraft (PHK) dissolving pulp (Enocell, 406 mL g^{-1}, 93.2% cellulose and 6.3% hemicelluloses; M_w = 131.05 kDa, M_n = 52.16 kDa, PDI = 2.51, DP < 100 = 6.08%, DP > 2000 = 7.38%; brightness = 90.8%) from Stora Enso (Finland) was provided in sheets and ground into a fine powder using a Fritsch mill. [DBNH][OAc] was synthesized by slowly adding an equimolar amount of acetic acid (100%, $C_2H_4O_2$, CAS: 64-19-7, M: 60.06 g mol^{-1}, Merck, Germany) to 1,5-diazabicyclo[4.3.0]non-5-ene (99%, DBN, $C_7H_{12}N_2$, CAS: 3001-72-7, M: 124.19 g mol^{-1}, abcr GmbH, Germany) at 70 °C, while stirring continuously to prevent the ionic liquid from solidifying.[31] Origin software[41] was used for the creation of the numerical graphs in the Results and discussion section.

Dope preparation and rheology

Cellulose solutions, also called dopes, of 13 wt% dry pulp consistency were prepared by direct dissolution of the pulp in melted [DBNH][OAc] in a vertical kneader at 80 °C under constant stirring (30 rpm) and vacuum pressure (<100 mbar). After 120 minutes, the remaining impurities and undissolved solids were removed by filtering the dopes using a hydraulic

filtration unit (metal filter, 6 μm nominal mesh size) at 80 °C and 180 bar.[42] The rheological properties of the solutions were investigated using an Anton Paar Physica MCR 302 rheometer equipped with a 25 mm parallel-plate geometry and 1 mm gap. Oscillatory shear measurements from 60 to 90 °C, with a 1% shear strain and a frequency range of 0.01 to 100 rad s^{-1} were preformed to determine the storage modulus (G'), loss modulus (G'') and complex viscosity (η^*).[43] Anton Paar Rheocompass software was used to calculate the crossover points of the dynamic moduli ($G' = G''$) for each temperature[44] and the zero-shear viscosity (η_0^*), following the Cross model and assuming the validity of the Cox–Merz rule.[45] The flow curve of a cellulose dope was measured using a capillary rheometer to cover high shear rates. The viscosity under high shear was measured using a Netzsch Rosand RH7 capillary rheometer equipped with a two-bore system consisting of a capillary die and an orifice die, which was used to correct the entrance pressure drop using the Bagley correction,[46] ensuring accurate measurement of the true shear stress. The capillary die had a diameter of 1 mm and a length of 20 mm, while the orifice die had the same diameter with a length of 0.25 mm. The cellulose solution was shaped into cylinders with a diameter of 1–1.5 mm and solidified in a refrigerator before loading into the barrel of the rheometer. Measurements with the capillary rheometer were performed at 75 °C across a shear rate range from 20 to 10 000 s^{-1}. The pressure drop across both dies was recorded, and the apparent viscosity was calculated using the Hagen–Poiseuille equation. Additionally, the Rabinowitsch–Weissenberg correction[47] was applied to account for the non-Newtonian nature of the dope, adjusting the apparent shear rate to the true shear rate.

Film production

The cellulose solutions were converted into films by the use of a customized dry-jet wet spinning unit (Fourné Polymertechnik, Germany) described initially by Sixta *et al.* for the production of textile fibres, and further optimized to create films in our previous work.[30,31] The dope was positioned in a vertical cylinder at 80 °C and melted before the targeted spinning temperature (75–85 °C) was adjusted. The solution then passed a triple layer filter plate (280/170/100 mesh), a breaking plate, a distribution plate in some cases, and was extruded through different slit nozzles at a rate of 0.229 m min^{-1}. The films coagulated upon immersion in a cold water bath (10–14 °C) after passing a 1 cm air gap and were guided to a motor-driven Teflon collecting roll at a speed of 0.723 m min^{-1}, providing a draw ratio (DR = collecting speed/extrusion speed) of 3.2. Afterwards, the films were washed to remove the remaining ionic liquid and dried following two different methods. Small batches of films were attached to a smooth glass surface, submerged in a water bath at 60 °C for 30 minutes and dried in an oven for 25 minutes at 40 °C. For films of at least 20 meters, a continuous washing and drying unit was designed and constructed to simulate a continuous industrial process.

Three spinnerets of different geometry (Table 1 and Fig. S1–S3†) and three distribution plates (Table S1 and Fig. S4†), provided by Elmer GmbH, Austria, were tested and their effects on the produced film properties were analysed. For each different combination of the spinnerets, both with and without DPs, three separate extrusion trials were performed. The spinnerets were not tempered and, instead, were heated passively through the cylinder and the spin dope flowing throw them.

Continuous washing and drying

A commercial roll-to-roll film production requires a continuous washing and drying set-up following the film extrusion unit operation. For this reason, a simplified industrial-like continuous washing and drying line operating under constant stretch was designed and constructed (Fig. 1). Regenerated cellulose films are extruded and collected for 30 to 60 min (20 to 40 m in total), and then placed immediately on a motor-driven feeding roll (b) located inside a 300 L water bath at 40–45 °C (a). The film passes through a set of freely rotating rolls until it reaches the heated drying drum at 40–45 °C (d) and is finally collected dry in a motor-driven collecting roll (e). The stability of the process is controlled by a tension control system (c), consisting of three freely rotating rolls situated outside of the water bath, where roll (2c) is equipped with a moving weighted arm (297.1 g) and a position sensor, while rolls (1c) and (3c) are used to stabilize the film. Water is continuously poured on top of rolls (1c), (2c), and (3c) to prevent the film from drying, which would not only deteriorate further ionic liquid removal, but would also create instabilities in the process due to differences in the stretchability between wet and dry films. All the rolls were 3D printed, except for the stainless-steel drying drum. The roll dimensions are gathered in Table S2.†

For process automatization, a software was developed to control the dimensions and direction of the motor-driven rolls, the process speed and the temperature of the drying drum. The speed of the process (up to 400 mm min^{-1}) is set by the collecting roll. The feeding speed is automatically adjusted depending on the position of the sensor of roll (2c). If roll 2c moves upwards, the film is overstretched due to the feeding roll (b) moving slower than the collecting roll (e). This is then counter-balanced by an increase in the feeding speed. Similarly,

Table 1 Geometry of the spinnerets studied (S4, S8 and S13) in comparison to the flat spinneret (FS) used in our previous work[30]

Spinneret code	Height (mm)	Length (mm)	Width (μm)	Entrance cone (°)	Capillary length (mm)
S4	16	70	250	4	2.4
S8				8	1.2
S13				13	0.3
FS[30]	1	60	250	90	1.0

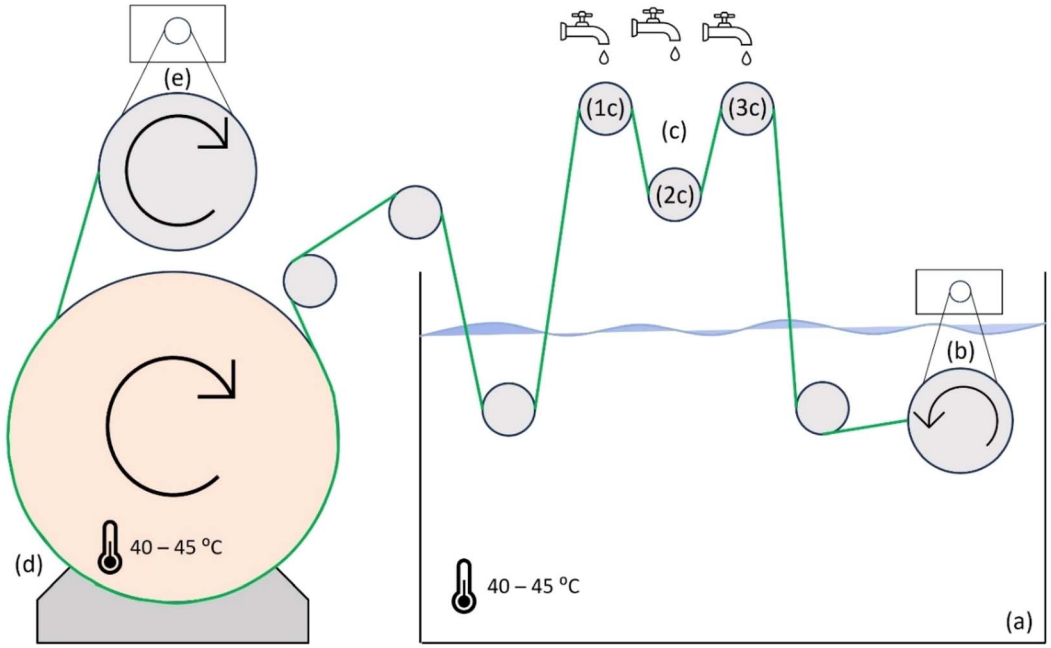

Fig. 1 Scheme of the continuous washing and drying unit, where (a) represents the water bath for the washing step, (b) the motor-driven feeding roll, (c) the tension control system, (d) the heated drying drum and (e) the motor-driven collecting roll.

if roll 2c moves downwards, meaning that collecting is slower than feeding, a decrease in the feeding velocity is triggered. This tension control and velocity adjustment is vital to ensure a constant and homogeneous stretch in the films.

Numerical simulation

The flow of the cellulose solutions through the spinnerets and distribution plates was simulated by COMSOL Multiphysics 6.2, a finite element software covering a wide range of different physics and engineering applications. Particularly, the Fluid Flow section of the software contains the Single-Phase Flow subsection with the Laminar Flow physics interface, which was assessed appropriate to describe the flow under scrutiny.

The finite element method breaks the region being analysed into smaller, regular subdomains called elements, and the entire collection of these elements forms a mesh. In the case of the flow of the dope through a spinneret, the finite element method solves the Navier–Stokes equations locally for each element and combines the local solutions into an approximative global solution. Hence, the solution flow velocities and shear rates distributions inside the spinneret were simulated, and the work done by shear forces on the dope was calculated as described in Section 6.1 of the ESI.†

Mechanical properties

The tensile properties of the spun cellulose films were measured according to the standard ISO 527-3:1995, with modifications made to the testing speed, and specimen and gauge lengths. These measurements were performed by the use of an MTS 400 tensile testing device using a 200 N cell and a speed test of 12 mm min^{-1}. The films were conditioned at 23 °C and 50% RH overnight preceding the measurements, and their thickness was determined by a Mitutoyo IP 65 micrometre, based on the ISO 4593:1993 standard. The samples were then cut into specimens with a fixed width of 15 mm and a length that depended on the direction of the measurement: for machine direction (MD; in direction of extrusion) tests, the specimen length was fixed to 100 mm and the gauge length for the measurement to 60 mm, whereas for transversal direction (TD; perpendicular to the direction of extrusion), the sample length depended on the width of the original film and the gauge length was set to 20 mm. For each sample, five specimens were tested. The Young's Modulus and toughness[48] were calculated using Matlab.[49] For the data analysis, the Grubbs' test was applied to identify outliner values.[50]

Wide angle X-ray scattering (WAXS)

The X-ray diffraction patterns of the films were recorded in transmission mode at reduced pressure (P = 0.2 mbar) by means of a Xenocs Xeuss 3.0 CuKα X-ray instrument (50 kV, 0.6 mA and λ = 1.5406 Å). The device was equipped with a 2D Dectris Eiger2 R 1M detector, with a detector-to-sample distance of 56 mm. The data was then processed using pyFAI software package[51] and the Hermans' orientation factor and crystallinity index were calculated as described earlier.[30] A blank run was performed to determine the background profile ($I_{bkg}(\theta)$), which was then employed to smoothen the recorded scattering profiles with a Savitzky–Golay filter and to calculate the crystallinity index (CI):

$$CI = \frac{\int I(\theta)d\theta - \int I_{bkg}(\theta)\, d\theta}{\int I(\theta)d\theta} \quad (1)$$

The azimuthal intensity profile of the diffraction peak (110), preferred orientation for regenerated cellulose II, together with the overlapping (110)/(020),[52] was fitted by a Pseudo–Voigt function, and then the orientation distribution between the (110) lattice plane (ϕ_{110}) and the fibril axis was calculated:

$$\langle \mathrm{Cos}^2\ \phi_{110} \rangle = \frac{\int_0^{\pi/2} I(\phi_{110}) \sin\ \phi_{110}\ \cos^2\ \phi_{110}\ \mathrm{d}\phi}{\int_0^{\pi/2} I(\phi_{110}) \sin\ \phi_{110}\ \mathrm{d}\phi} \quad (2)$$

which was then converted to the disorientation between the fibril and the crystallographic *c*-axis:

$$\langle \mathrm{Cos}^2\ \phi \rangle_c = 1 - 2\ \langle \cos^2\ \phi \rangle_{110} \quad (3)$$

Lastly, the Hermans' orientation factor was determined:

$$f_{\mathrm{WAXD}} = \frac{3\langle \cos^2\ \phi \rangle_c - 1}{2} \quad (4)$$

Transparency

The optical transmittance of the films was measured in the visible light spectrum, 400–800 nm, by a Shimadzu UV-2600 spectrophotometer.[53]

Washing efficiency

The amount of residual nitrogen in the films is correlated with the efficiency of the washing step to remove the ionic liquid from the samples. It was monitored *via* elemental analysis using a Thermo Fisher Flash Smart CHNSO Elemental Analyzer with helium as a carrier and sulphanilamide ($C_6H_8N_2O_2S$, CAS: 63-74-1, M: 172.2 g mol^{-1}, N = 16.29%, C = 41.81%, H = 4.65%, Merck, Germany) as standard, in accordance with the standard EN 15104:2011.

Results and discussion

Rheology of the cellulose solutions

The rheological properties of the cellulose solutions, governed by the concentration and temperature of the dope, have been proven as a significant factor for the extrusion stability and the properties of the final products, for both fibres and films.[30,31,37] For the production of high-quality films from 13 wt% cellulose solutions, the optimum zero-shear viscosities were in the range of 8000 to 19 000 Pa s and cross-over points (COP) of 3900–4200 Pa at angular frequencies of 1.3 to 3.4 s^{-1}.[30] Therefore, for this study films were extruded at temperatures from 75 to 85 °C, which corresponded to zero-shear viscosities of 14 600 ± 700 to

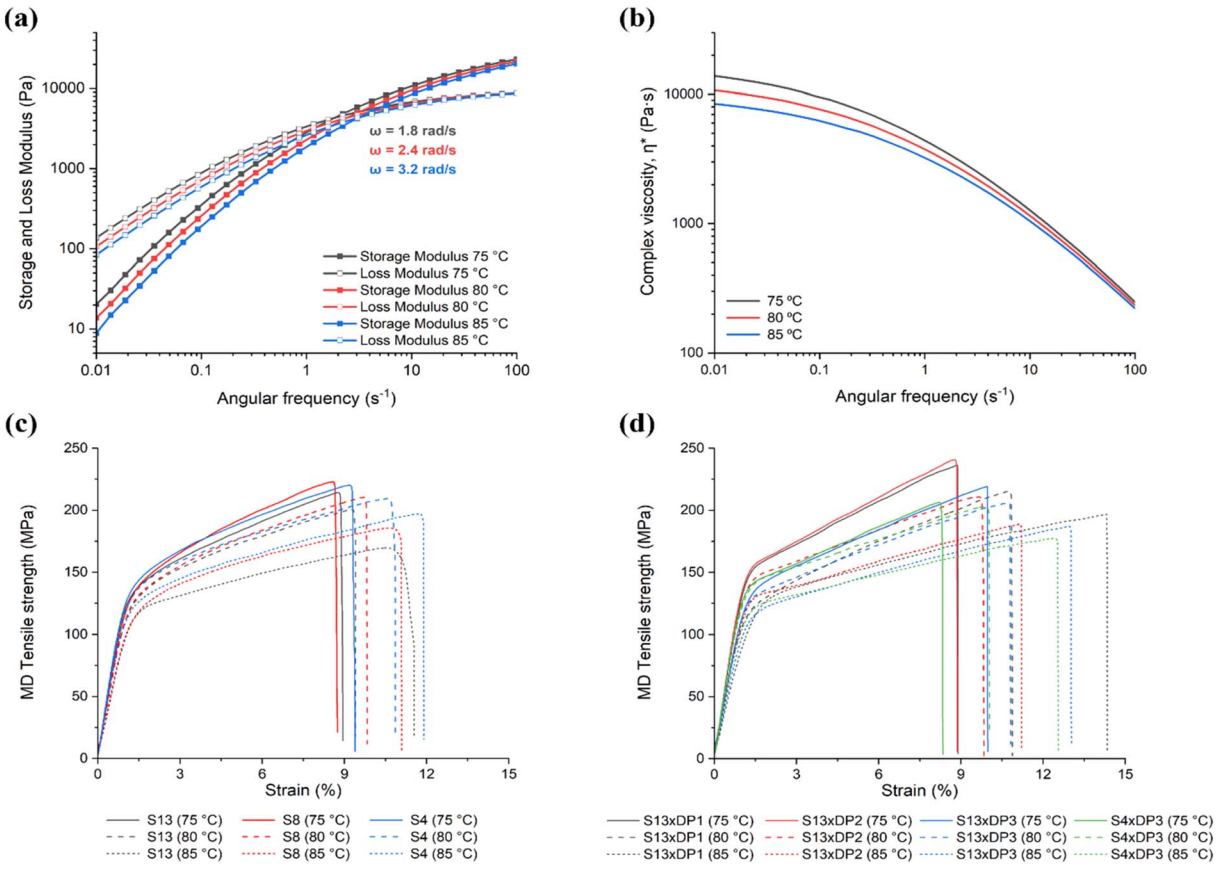

Fig. 2 (a) Double-logarithmic plot of the loss and storage moduli, and (b) complex viscosities (η^*) of the 13 wt% cellulose solutions at angular frequencies from 0.01 to 100 s^{-1}, at the extrusion temperatures. (c) Stress–strain curves in MD of films produced by the use of spinneret S13 (black), S8 (red) and S4 (blue), without distribution plate, from 13 wt% cellulose solutions at the different spinning temperatures. (d) Stress–strain curves of films produced using a combination of spinneret S13 and distribution plate DP1 (black), S13 and distribution plate DP2 (red), S13 and distribution plate DP3 (blue), and spinneret S4 and distribution plate DP3 (green), from and 13 wt% cellulose dopes at the extrusion temperatures.

8800 ± 400 Pa s and a COP of 4300–4400 Pa at angular frequencies of 1.8 to 3.2 s^{-1} (Fig. 2a and b).

The mathematical simulations of the flow of a 13 wt% dope through the spinnerets were based on its shear viscosity at shear rates from 0.01 to 35 000 s^{-1} and at 75 °C, fitted to a cross-fluid model (Fig. S5†).

Effect of the spinneret geometry on the extrusion stability and mechanical properties

The effect of the spinneret geometry on the extrusion speed was evaluated by controlling the spinning temperature to maintain a constant zero-shear viscosity of the dopes. When a flat spinneret without entrance cone (Table 1) was used, the maximum extrusion velocity was low. Speeds above 0.133 m min^{-1} led to melt fracture, caused by high shear rates between the dope and the spinneret walls, which resulted in deformations on the surface of the extrudate, also known as shark skin.[30,54–56] With this geometry, films could be collected at a constant speed of 0.356 m min^{-1} (DR = 2.7). In contrast to these observations, the conical geometry of the nozzle slits examined in this study (Table 1 and Fig. S1–S3†) allowed for up to six times higher extrusion rates without negatively affecting the surface of the films. However, higher extrusion and, consequently, higher take-up velocities, were partly impeded due to technical limitations posed by the laboratory-scale coagulation bath and motor-driven collecting roll. Instabilities were encountered at high take-up velocities. Thus, all experiments in this study were conducted at an extrusion speed of 0.229 m min^{-1} and production speed of 0.723 m min^{-1} (DR = 3.2).

In our previous study using a flat spinneret, thin (12–21 μm) and homogeneous films were obtained, with stress values in MD up to 142 MPa with 9% elongation at break from a 13 wt% cellulose solution, and up to 210 MPa and 8% elongation at break with an 8 wt% dope.[30] These properties already surpassed those of commercial uncoated cellophane, which presents stress values of 125 MPa and 22% elongation with a film thickness between 21–31 μm.[11] Herein, by the introduction of spinnerets with an entrance cone before the spin capillary, the mechanical properties (Tables 2 and S3†) could be further improved.

The spinnerets with three different conical entrance channels (S4, S8 and S13) were designed to have a more uniform flow of the solution, which supports the alignment of the cellulose chains during the extrusion process. Within the studied range of entrance cone angles no significant effect on the mechanical properties was observed for solutions with high viscosities (14 600 ± 700 Pa s). However, having an entrance cone was clearly beneficial for the strength of the films, that reached values of 218–226 MPa with 9% elongation, when spun at 75 °C. When extruding solutions at low viscosity (8800 ± 400 Pa s), spinneret S4 led to films with the highest mechanical properties (192 ± 3 MPa and 13 ± 1% elongation at break), while those extruded with S13 exhibited the lowest (175 ± 6 MPa and 12 ± 1% elongation at break). This suggests that at low viscosities, the alignment of the cellulose chains in the final film is improved by smaller entrance cones. At low viscosity (high temperature)

Table 2 Mechanical properties, crystallinity and Hermans orientation of the films extruded *via* the spinnerets with different geometries and at different temperatures (MD = machine direction, TD = transversal direction, ± represents 95% confidence interval). All films were produced from 13 wt% cellulose solutions without distribution plate (DP)

Spinning temperature (°C)	Zero-shear viscosity (Pa s)	Spinneret	Thickness (μm)	Crystallinity (%)	Hermans orientation factor	MD tensile strength (MPa)	MD strain (%)	MD Young's modulus (GPa)	MD toughness (MPa)	TD tensile strength (MPa)	TD strain (%)	TD Young's modulus (GPa)	TD toughness (MPa)
75	14 600 ± 700	S4	16 ± 1	35.03 ± 0.24	0.52 ± 0.01	218 ± 6	9 ± 1	13 ± 0.6	16 ± 1	73 ± 2	27 ± 4	4 ± 0.1	22 ± 3
		S8	16 ± 1	34.77 ± 0.24	0.54 ± 0.02	226 ± 5	9 ± 1	14 ± 0.4	15 ± 1	74 ± 1	29 ± 3	4 ± 0.1	24 ± 2
		S13	16 ± 1	35.50 ± 0.30	0.55 ± 0.03	218 ± 8	9 ± 1	14 ± 0.5	15 ± 2	71 ± 4	29 ± 4	4 ± 0.2	22 ± 3
80	11 100 ± 500	S4	15 ± 1	34.70 ± 0.11	0.44 ± 0.01	203 ± 5	12 ± 1	12 ± 0.7	19 ± 1	77 ± 2	34 ± 6	4 ± 0.1	29 ± 4
		S8	16 ± 1	34.73 ± 0.62	0.47 ± 0.03	209 ± 4	10 ± 1	12 ± 0.4	16 ± 1	75 ± 2	31 ± 3	3 ± 0.1	26 ± 3
		S13	15 ± 1	35.43 ± 0.43	0.43 ± 0.02	203 ± 5	9 ± 1	13 ± 0.3	16 ± 1	77 ± 2	34 ± 3	4 ± 0.1	29 ± 2
85	8800 ± 400	S4	15 ± 1	34.73 ± 0.17	0.35 ± 0.01	192 ± 3	13 ± 1	12 ± 0.9	21 ± 2	79 ± 2	40 ± 3	4 ± 0.1	34 ± 2
		S8	15 ± 1	35.10 ± 0.41	0.39 ± 0.02	184 ± 3	11 ± 1	11 ± 0.4	16 ± 1	81 ± 2	32 ± 4	3 ± 0.1	29 ± 3
		S13	15 ± 1	35.47 ± 0.07	0.39 ± 0.01	175 ± 6	12 ± 1	11 ± 0.5	18 ± 1	83 ± 4	40 ± 3	4 ± 0.2	36 ± 2

the average relaxation time for the cellulose chains in solution is shorter. Thus, shear induced orientation can get lost before the structured solution is coagulated in the spin bath. A lower entrance cone angle results in relative higher shear stress and strain (Fig. 3a). Within the time that the extruded films need to pass the air gap, the oriented cellulose chain relax to a lesser extent and the orientation is preserved in the films. Regardless of the spinning viscosity, all the films produced with the conical spinnerets from 13 wt% cellulose solutions exhibited between 29 and 58% higher tensile strength compared to the previous research.[30]

In the air gap, the films are stretched in longitudinal direction but not in transversal direction, which leads to anisotropic mechanical properties. The mechanical properties in TD followed an inverse trend compared to the MD values: films produced at higher temperatures displayed slightly higher tensile strength and strain values (79–83 MPa with 32–40% elongation at 85 °C) compared to those extruded at lower temperatures (71–74 MPa with 27–29% elongation at 75 °C). In any case, the stress–strain behaviour is reproducible with small data scattering for all temperatures and spinnerets examined. In contrast, films spun from 13 wt% solutions through a FS spinneret showed TD values between 50 and 88 MPa with 13–34% elongation (Table S3†), when extruded at high and low viscosities, respectively.[30] In other words, the values in TD displayed high standard deviations illustrating inhomogeneities in the film production. The new spinneret design helped to overcome this issue.

All produced films illustrated a cellulose II pattern (Fig. S6†), with peaks at 12.2° (1–10), 19.9° (110), 21.6° (020) and 35.2° (004).[57] The Hermans orientation factor and the crystallinity index of the films generated by the three conical spinnerets, without distribution plate, are summarized in Table 2. By increasing the dope zero-shear viscosity from 8800 to 14 600 Pa s, the MD tensile strength enhances from 175 to 226 MPa at the same time as the orientation of the films improves from 0.38 to 0.54. In contrary, the MD strain diminishes from 13 to 9%. As mentioned earlier, a high viscosity (low temperature) of the solution during spinning leads to more oriented structures, and therefore, stronger but stiffer films with reduced elongation at

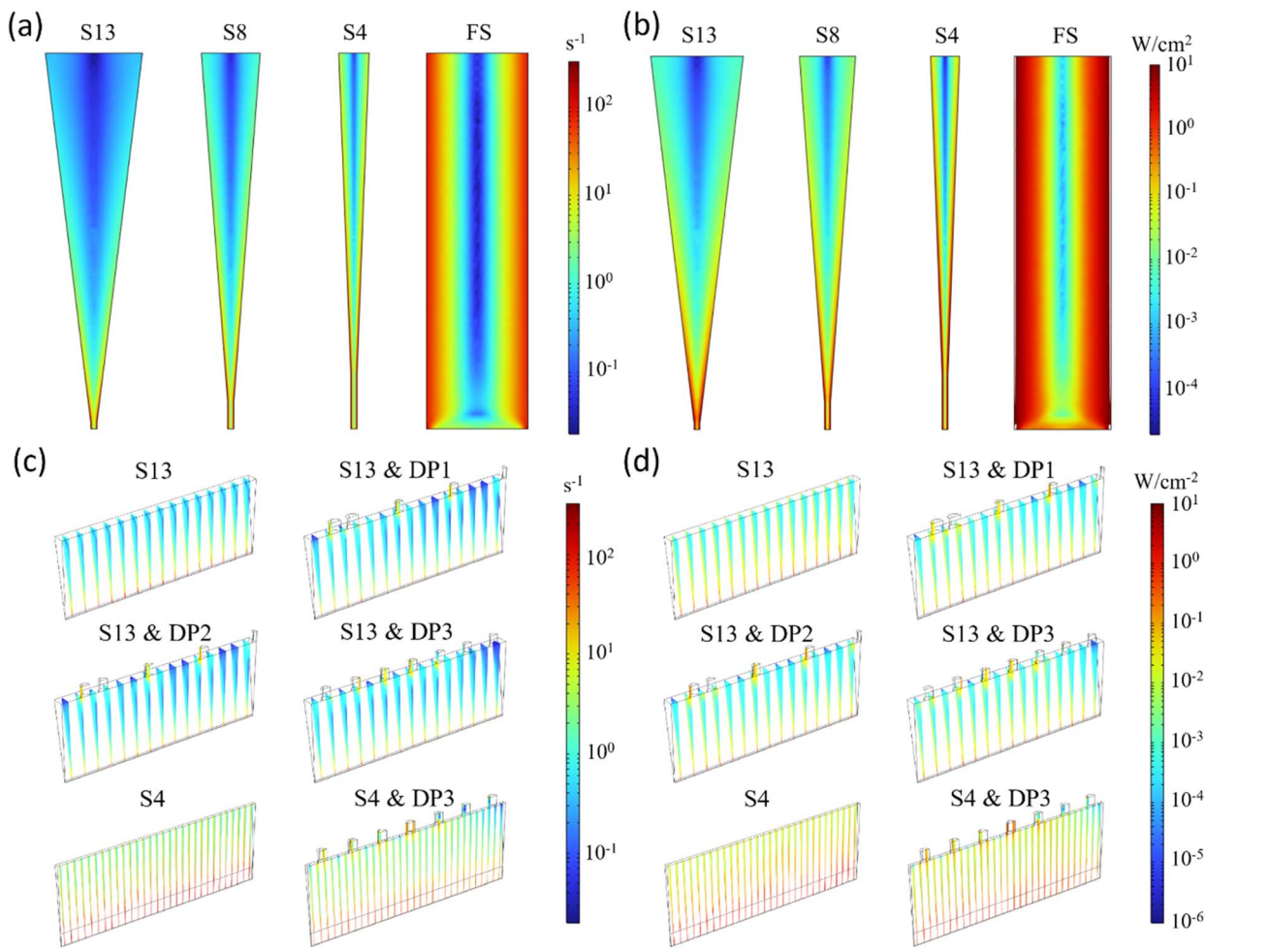

Fig. 3 (a) Simulated shear rates and (b) shear power densities of the conical spinnerets (S13, S8 and S4), in comparison to the flat spinneret (FS). It is important to note that FS is not in scale with the others: the diameter is much smaller (Table 1). (c) Simulated shear rates and (d) power distributions of the entrance cone and channel in S13 and S4 with and without the studied DPs. Only half of the length of cone and channel are plotted because of their mirror symmetry.

break. Furthermore, as orientation increases, the lateral interaction between crystallites decreases, leading to a loss in transversal strength.

The flow of the cellulose solution through the conical and flat spinnerets has been simulated to gain a better understanding of the internal stress acting on the dope. The spinnerets used in this study all have extrusion channels with a high L/D-ratio, that is the length of the channel is several times greater than the width (Fig. S3† and Table 1). Because of this, we may assume that the flow remains constant along the length direction of the spinneret. Therefore, the calculations can be simplified to a two-dimensional cross-section parallel to the two vertical surfaces that define the geometry's lateral boundaries. Combining the data obtained with the plate–plate and the capillary rheometers, it was possible to fit the viscosity data of the 13 wt% dope spanning six orders of magnitude of shear rate with the cross-fluid model (Fig. S5†). This fit allowed for the simulation of the flow velocity distributions in the spinneret channel, illustrated in Fig. S7.†

In the case of dry-jet wet filament spinning, cellulose chain orientation is predominantly determined by the draw of the filaments in the air gap.[37] In addition, the shear stress inside the spin capillaries can induce chain pre-alignment,[40] resulting in a transition from a random-coil conformation into one that is more aligned with the streamlines in the entrance cone and spin capillary (Fig. S8†).

A study on the simulation of the flow inside spinnerets with entrance angles ranging from 40 to 90° for the production of fibres reported that angles over 40° created "dead zones", regions where the dope flow was impaired, reaching the biggest "dead region" when a 90° entrance cone was used.[58] The entrance angle of the conical spinnerets examined herein are significantly smaller than 40°, therefore the shear rates inside them are more homogeneous, as illustrated in Fig. 3a. The flat spinneret described in our previous work could be considered as 90° entrance cone, which would explain the lower chain orientation and flow instabilities observed at higher extrusion speed.

Among the conical spinnerets, S4 presents higher shear rates, and therefore, shear powers (Fig. 3b and Table S4, see ESI 6.1† for definition), along the walls of the spinneret. This might not have a significant effect on the chain orientation compared to S8 and S13 at high viscosities, but it might explain the higher tensile values obtained at lower dope viscosity, as observed in Table 2.

Effect of the distribution plates in the film spinnability and mechanical properties

When applying draw onto a film in the air gap, the elongation in longitudinal direction causes a contraction in transversal direction. The contraction causes structural changes along the film width, which can affect the mechanical properties of the final film. Therefore, a set of three distribution plates were crafted in a further attempt to have a better control of the cellulose solution flow inside the spinneret and the air gap, to possibly obtain higher cellulose chain orientations, and

Table 3 Crystallinity index, Hermans orientation factor and mechanical properties of the films obtained when using a combination of the spinnerets S13 and S4 with different distribution plates (DP1, DP2 and DP3), at the indicated spinning temperatures (MD = machine direction, TD = transversal direction, ± represents 95% confidence interval)

Spinning temperature (°C)	Zero-shear viscosity (Pa s)	Spinneret + distribution plate	Thickness (μm)	Crystallinity (%)	Hermans orientation factor	MD tensile strength (MPa)	MD strain (%)	MD Young's modulus (GPa)	MD toughness (MPa)	TD tensile strength (MPa)	TD strain (%)	TD Young's modulus (GPa)	TD toughness (MPa)
75	14 600 ± 700	S13-DP1	13 ± 1	35.97 ± 0.40	0.59 ± 0.01	239 ± 12	9 ± 1	15 ± 0.3	22 ± 2	67 ± 2	21 ± 6	4 ± 0.4	15 ± 4
		S13-DP2	15 ± 1	35.87 ± 0.13	0.57 ± 0.01	242 ± 12	10 ± 1	15 ± 0.2	18 ± 3	71 ± 2	19 ± 3	4 ± 0.1	15 ± 3
		S13-DP3	17 ± 1	35.77 ± 0.13	0.55 ± 0.01	217 ± 6	10 ± 1	13 ± 0.3	17 ± 3	69 ± 2	25 ± 4	3 ± 0.1	19 ± 3
		S4-DP3	16 ± 1	35.73 ± 0.17	0.52 ± 0.01	206 ± 4	8 ± 1	14 ± 0.4	14 ± 1	68 ± 2	19 ± 2	4 ± 0.1	15 ± 2
80	11 100 ± 500	S13-DP1	13 ± 1	36.17 ± 0.13	0.52 ± 0.02	213 ± 9	11 ± 2	12 ± 1	17 ± 3	71 ± 2	24 ± 6	4 ± 0.3	19 ± 4
		S13-DP2	14 ± 1	35.67 ± 0.07	0.48 ± 0.01	221 ± 10	10 ± 2	14 ± 0.5	17 ± 3	73 ± 2	22 ± 3	4 ± 0.1	19 ± 2
		S13-DP3	16 ± 1	35.67 ± 0.17	0.51 ± 0.01	205 ± 11	11 ± 1	12 ± 0.5	18 ± 3	72 ± 1	28 ± 6	4 ± 0.1	22 ± 4
		S4-DP3	15 ± 1	35.37 ± 0.07	0.46 ± 0.01	197 ± 9	10 ± 1	13 ± 0.8	16 ± 2	75 ± 2	29 ± 3	4 ± 0.2	24 ± 3
85	8800 ± 400	S13-DP1	13 ± 1	36.07 ± 0.07	0.49 ± 0.01	200 ± 14	14 ± 1	11 ± 2	17 ± 3	72 ± 2	25 ± 6	4 ± 0.1	21 ± 4
		S13-DP2	15 ± 1	35.47 ± 0.07	0.41 ± 0.01	187 ± 3	11 ± 1	12 ± 0.5	16 ± 1	75 ± 2	28 ± 4	4 ± 0.1	25 ± 4
		S13-DP3	16 ± 1	35.53 ± 0.17	0.41 ± 0.01	185 ± 5	13 ± 1	11 ± 0.3	21 ± 3	73 ± 4	31 ± 8	4 ± 0.2	28 ± 7
		S4-DP3	15 ± 1	35.63 ± 0.07	0.36 ± 0.01	174 ± 7	12 ± 1	11 ± 0.5	17 ± 1	79 ± 2	35 ± 6	4 ± 0.1	31 ± 5

stronger and wider films. The number, dimensions, and distances of the holes (Fig. S4 and Table S1†) control the supply of dope across the length of the spin channel. The effects on the mechanical properties, film thickness and morphology are collected in Table 3.

The use of the distribution plates certainly influenced the cellulose chain orientation and tensile properties. When spun at 75 °C, the combination of S13 and DP1 generated films with tensile strength up to 239 MPa and 9% elongation at break, 10% stronger than the films produced by S13 without any distribution plate. The use of DP2 with S13, marginally increased the average tensile strength to 242 MPa and 10% elongation. However, with both combinations two issues arose. First, they led to unstable extrusion due to the introduction of air bubbles in the dopes, which caused the formation of small holes across the entire continuous films; and second, the thickness of the films showed a higher variation. The two exterior holes on each side of DP1 and DP2 (Fig. S4†) were expected to improve the width of the films due to the increased amount of dope on the sides of the spinnerets. However, it caused the films to be thicker on the sides compared to the centre. The thickness values in Table 3 corresponded to measurements performed at the centre of each film. The later issue was solved with DP3, which increased the flow by adding more equidistantly positioned holes and led to films with homogeneous thickness. The air bubbles in the dope, however, increased, worsening the extrusion stability to the point of breakages during the film collection. Regarding the mechanical properties, the created films exhibited the same stress values (217 MPa), with only a small increase in elongation (10%) compared to the films spun without the distribution plate. Reducing the cone size from S13 to S4 in combination with DP3 showed no improvements. The mechanical properties declined in strength and elongation in MD (206 MPa and 8% elongation at 75 °C). The stress–strain behaviour in machine direction of the films generated by the use of the DPs is illustrated in Fig. 2d. For all combinations of spinneret and DPs examined, the stress–strain behaviour in transversal direction were not greatly affected and were in the same range as the films produced without DP.

When DPs are used, the previous assumption of uniform flow over the length of the spinneret is no longer valid and a third dimension must be added to the simulation of the flow. Fig. 3c and d show the simulated shear rates and shear power densities in the 13° and 4° spinnerets, respectively, with and without the flow regulating plate at the inlet. The entrance holes in the distribution plates result in a decrease in the shear forces, causing an interruption of the flow and further the introduction of defects in the films during the spinning.

The geometry of the studied spinnerets and the use of distribution plates did not influence the crystallinity values of the films (35–36%), which was in line with the films analysed in our previous work (34–38%) and with Ioncell® fibres reported earlier (32–36%).[30,40,59] The introduction of the distribution plates generated films with slightly higher orientation factors (up to 0.59) than the films produced without them (0.54), which align with the small increase in the tensile strengths (242 MPa and 226 MPa, respectively).

Continuous washing and drying

The optimum washing and drying velocity, set by the collecting roll, was found to be 375–385 mm min^{-1} for this set-up. This speed provided completely washed and dried films.

The effect of the water bath temperature and the length of the washing path on the washing efficiency was studied. In our previous work, 60 °C was the lowest temperature that removed the ionic liquid effectively from the films, without affecting the shape, when washed attached to a glass surface and immersed in a small water bath.[30] Therefore, temperatures from 40 to 60 °C were tested in the continuous washing line, and the films were then subjected to elemental analysis to measure the residual nitrogen content. Due to the bigger volume of water, a temperature of 40 °C is enough for efficient removal of the ionic liquid from the films.

The length of the washing path is an important factor when scaling-up and dimensioning the equipment. The shortest possible path that successfully removed the IL from the films had a total of 225 cm (5.8–6.0 min), where 72 cm (1.9 min) were inside the water bath.

Lastly, the drying process starts instantly when the films leave the water and continues for 292 cm (7.6–7.8 minutes). The films were guided towards the drying drum, where they were attached to for a total of 184 cm (4.8–4.9 min). The drum surface

Table 4 Mechanical properties, thickness, width, transmittance and elemental analysis values of the films produced with spinneret S13, without using a distribution plate, when washed and dried manually and in continuous mode, respectively

Properties		Films – manual washing	Films – continuous washing and drying	Initial PHK pulp
Mechanical properties	MD stress (MPa)	218 ± 8	219 ± 5	—
	MD strain (%)	9 ± 1	8 ± 1	—
	TD stress (MPa)	71 ± 4	62 ± 1	—
	TD strain (%)	29 ± 4	23 ± 3	—
Thickness (μm)		16 ± 1	17 ± 1	—
Film width (cm)		3.5 ± 0.1	3.1 ± 0.1	—
Transmittance at 800 nm (%)		91.17 ± 0.13	88.80 ± 0.47	—
Elemental analysis	N (%)	0.078 ± 0.005	0.073 ± 0.007	0.010 ± 0.001
	C (%)	39.88 ± 0.42	40.10 ± 0.41	41.86 ± 0.02
	H (%)	6.25 ± 0.07	6.23 ± 0.08	6.22 ± 0.06

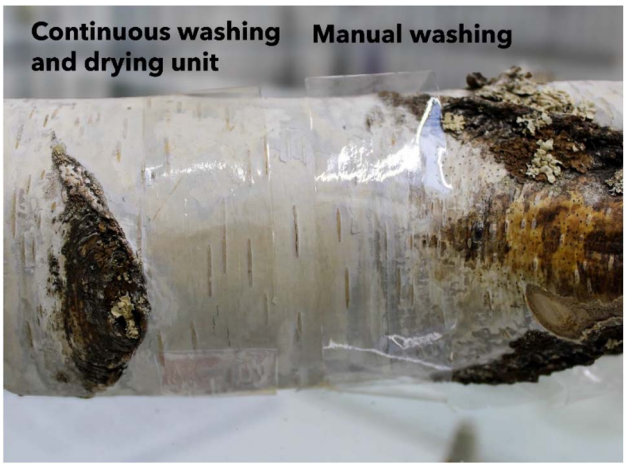

Fig. 4 Photograph of the films washed and dried by the use of the continuous unit (left) and manually (right) over a wood log.

was evenly heated to 40–45 °C,[30] and was driven by the collecting roll (e). The drying temperature was adjusted, depending on the ambient temperature and the relative humidity.

In summary, the optimal conditions for the continuous washing and drying unit were a speed of 375–385 mm min^{-1}, a temperature of the water bath and the drying drum of 40–45 °C, a length of 72 cm inside the water bath, and a drying length of 292 cm. Table 4 gathers the properties of the films produced with spinneret S13, without a distribution plate, at 75 °C when they were washed and dried either manually off-line or in continuous mode. The thickness (16–17 μm) and the mechanical properties were not affected by the automated system in longitudinal direction (218–219 MPa), and only slightly in transversal (71–62 MPa). However, some shrinking was observed in the film widths (3.1–3.5 cm), resulting from the constant stretch of the films along the continuous line. Regarding the film transparency, the films from the washing and drying line exhibited a slightly lower transmittance value (88.8%) compared to the off-line films (91.2%), due to the friction of the films with the drying drum during the drying step. Regardless, the transparency is still very high, as shown in Fig. 4, and in the same range of cellophane.[22,60,61] Lastly, the automated washing line also demonstrated high efficiency, as the residual nitrogen content within the films is lower than when they are washed manually.

Conclusions

In this study, the influence of the spinneret geometry and the flow inside the spinneret on the morphology and mechanical properties of the cellulose films was assessed. A mathematical simulation was performed to support the understanding of the flow behaviour of the cellulose solution. For 13 wt% dopes, the films produced through spinnerets with a conically shaped entrance cone prior to the capillary channel (entrance angle of 4, 8 and 13°) presented a great increase in orientation and up to 58% higher strength compared to the films obtained in our previous work with a flat (entrance angle 90°) spinneret (142 to 226 MPa). The numerical simulation showed that the entrance cones led to higher shear rates and power inside of the spinnerets, leading to a higher orientation of the cellulose chains parallel to the shear stress tensor. This pronounced molecular orientation was preserved in the resulting coagulated films, in particular at higher extrusion temperatures, that is lower solution viscosities. Moreover, the addition of distribution plates slightly improved the chain orientation of the films and their mechanical properties (up to 242 MPa) when combined with S13, but the extrusion stability was impaired. Further optimization of the hole number, dimensions and distribution in the distribution plate could prevent the formation of air pockets which led to the extrusion instabilities and defects in the final films. Lastly, a continuous line for washing and drying the films was constructed and optimized. The residual IL was removed efficiently, and the resulting films exhibited very high transparency, similar thickness, and equal mechanical properties as the films washed off-line.

Data availability

The data supporting the findings of this research is available in the ESI† of this article.

Author contributions

Eva González Carmona: conceptualization, methodology, investigation, visualization, writing – original draft, funding acquisition. Inge Schlapp-Hackl: conceptualization, supervision, methodology, investigation, writing – review and editing. Kaarlo Nieminen: methodology, formal analysis. Wenwen Fang: formal analysis. Seppo Jääskeläinen: resources. Kalle Salonen: software. Hannes Elmer: resources. Helena Westerback: visualization. Michael Hummel: conceptualization, supervision, writing – review and editing. Herbert Sixta: supervision, writing – review and editing.

Conflicts of interest

The authors declare that Hannes Elmer is a commercial producer of spinnerets and provided the design of the studied slit nozzles, but did not influence the study design, data collection, or interpretation of results.

Acknowledgements

Eva González Carmona gratefully acknowledges funding from the Jenni and Antti Wihuri Foundation (Project Numbers 00220062 and 00230076). The authors acknowledge the provision of facilities and technical support by Aalto University at OtaNano – Nanomicroscopy Center (Aalto-NMC). Additionally, the authors want to acknowledge Daisuke Sawada for the python code employed in the analysis of the XRD data.

References

1 Plastics Europe AISBL, *Plastics - The Fast Facts 2023*, Belgium, 2023.
2 OECD, *Global Plastics Outlook: Policy Scenarios to 2060*, OECD Publishing, Paris, 2022.
3 N. Laskar and U. Kumar, *Environ. Technol. Innovation*, 2019, **14**, 100352.
4 G. G. N. Thushari and J. D. M. Senevirathna, *Heliyon*, 2020, **6**, e04709.
5 Plastics Europe AISBL, *Plastics - The Fast Facts 2024*, Belgium, 2024.
6 European Commission, *Directive (EU) 2019/904 of the European Parliament and of the Council of 5 June 2019 on the reduction of the impact of certain plastic products on the environment*, Official Journal of the European Union, 2019.
7 European Commission, *Commission notice—Commission guidelines on single-use plastic products in accordance with Directive (EU) 2019/904 of the European Parliament and of the Council on the reduction of the impact of certain plastic products on the environment*, Official Journal of the European Union, 2021.
8 G. C. Inskeep and P. Van Horn, *Ind. Eng. Chem.*, 1952, **44**, 2511–2524.
9 B. A. Morris, in *The Science and Technology of Flexible Packaging: Multilayer Films from Resin and Process to End Use*, Elsevier Inc., 2017.
10 H. P. Fink, P. Weigel, H. J. Purz and J. Ganster, *Prog. Polym. Sci.*, 2001, **26**, 1473–1524.
11 Futamura Group, Cellophane™ PT – Data Sheet, 2022, **https://www.futamuragroup.com/en/**, accessed February 2022.
12 R. O. Beauchamp, J. S. Bus, J. A. Popp, C. J. Boreiko, L. Goldberg and M. J. McKenna, *CRC Crit. Rev. Toxicol.*, 1983, **11**, 169–278.
13 M. Davidson and M. Feinleib, *Am. Heart J.*, 1972, **83**, 100–114.
14 S. Krstev, B. Peruničić, B. Farkić and R. Banićević, *J. Occup. Health*, 2003, **45**, 81–87.
15 H.-W. Kuo, J.-S. Lai, M. Lin and E.-S. Su, *Int. Arch. Occup. Environ. Health*, 1997, **70**, 61–66.
16 H. Sadeghifar, R. Venditti, J. J. Pawlak and J. Jur, *BioResources*, 2019, **14**, 9021–9032.
17 C. Zhou and Y. Wang, *J. Appl. Polym. Sci.*, 2021, **138**, 51255.
18 R. Yudianti, A. Syampurwadi, H. Onggo, M. Karina, H. Uyama and J. Azuma, *Polym. Adv. Technol.*, 2016, **27**, 1102–1107.
19 M. N. Nguyen, U. Kragl, I. Barke, R. Lange, H. Lund, M. Frank, A. Springer, V. Aladin, B. Corzilius and D. Hollmann, *Commun. Chem.*, 2020, **3**, 116.
20 J. Cao, W. Wei, G. Gou, M. Jiang, Y. Cui, S. Zhang, Y. Wang and Z. Zhou, *Cellulose*, 2018, **25**, 1975–1986.
21 Y. Xie, P. Cai, X. Cao and Y. Pan, *Ind. Crops Prod.*, 2024, **207**, 117768.
22 L. Zhang, D. Ruan and J. Zhou, *Ind. Eng. Chem. Res.*, 2001, **40**, 5923–5928.
23 P. Gspaltl, C. Schlossnikl, J. Kalleitner and H. Firgos, *PTC*, WO 99/63136, 1999.
24 P. Gspaltl and C. Schloss-Nikls, *PTC*, WO 00/24812, 2000.
25 G. Shanshan, W. Jianqing and J. Zhengwei, *Carbohydr. Polym.*, 2012, **87**, 1020–1025.
26 J. Pang, X. Liu, X. Zhang, Y. Wu and R. Sun, *Materials*, 2013, **6**, 1270–1284.
27 J. Pang, M. Wu, Q. Zhang, X. Tan, F. Xu, X. Zhang and R. Sun, *Carbohydr. Polym.*, 2015, **121**, 71–78.
28 J. Pang, X. Liu, M. Wu, Y. Wu, X. Zhang and R. Sun, *J. Spectrosc.*, 2014, **2014**, 1–8.
29 D. Wawro, M. Hummel, A. Michud and H. Sixta, *Fibres Text. East. Eur.*, 2014, **22**, 35–42.
30 E. González Carmona, I. Schlapp-Hackl, S. Jääskeläinen, M. Järvinen, K. Nieminen, D. Sawada, M. Hummel and H. Sixta, *Cellulose*, 2023, **30**, 11633–11648.
31 H. Sixta, A. Michud, L. Hauru, S. Asaadi, Y. Ma, A. W. T. King, I. Kilpeläinen and M. Hummel, *Nord. Pulp Pap. Res. J.*, 2015, **30**, 43–57.
32 A. Michud, M. Tanttu, S. Asaadi, Y. Ma, E. Netti, P. Kääriainen, A. Persson, A. Berntsson, M. Hummel and H. Sixta, *Text. Res. J.*, 2015, **86**, 543–552.
33 M. Hummel, A. Michud, M. Tanttu, S. Asaadi, Y. Ma, L. K. J. Hauru, A. Parviainen, A. W. T. King, I. Kilpeläinen and H. Sixta, in *Cellulose Chemistry and Properties: Fibers, Nanocelluloses and Advanced Materials*, ed. O. Rojas, Springer, Cham, 2015, ch. 307, vol. 271, pp. 133–168.
34 A. Parviainen, R. Wahlström, U. Liimatainen, T. Liitiä, S. Rovio, J. K. J. Helminen, U. Hyväkkö, A. W. T. King, A. Suurnäkki and I. Kilpeläinen, *RSC Adv.*, 2015, **5**, 69728–69737.
35 W. Ahmad, A. Ostonen, K. Jakobsson, P. Uusi-Kyyny, V. Alopaeus, U. Hyväkkö and A. W. T. King, *Chem. Eng. Res. Des.*, 2016, **114**, 287–298.
36 S. Elsayed, S. Hellsten, C. Guizani, J. Witos, M. Rissanen, A. H. Rantamäki, P. Varis, S. K. Wiedmer and H. Sixta, *ACS Sustainable Chem. Eng.*, 2020, **8**, 14217–14227.
37 A. Michud, M. Hummel and H. Sixta, *J. Appl. Polym. Sci.*, 2016, **133**, 43718.
38 L. K. J. Hauru, M. Hummel, A. Michud and H. Sixta, *Cellulose*, 2014, **21**, 4471–4481.
39 K. Moriam, D. Sawada, K. Nieminen, M. Hummel, Y. Ma, M. Rissanen and H. Sixta, *Cellulose*, 2021, **28**, 9547–9566.
40 K. Moriam, D. Sawada, K. Nieminen, Y. Ma, M. Rissanen, N. Nygren, C. Guizani, M. Hummel and H. Sixta, *Cellulose*, 2021, **28**, 11165–11181.
41 P. M. Edwards, *J. Chem. Inf. Comput. Sci.*, 2002, **42**, 1270–1271.
42 Y. Ma, S. Asaadi, L. S. Johansson, P. Ahvenainen, M. Reza, M. Alekhina, L. Rautkari, A. Michud, L. Hauru, M. Hummel and H. Sixta, *ChemSusChem*, 2015, **8**, 4030–4039.
43 A. Michud, M. Hummel, S. Haward and H. Sixta, *Carbohydr. Polym.*, 2015, **117**, 355–363.
44 T. G. Mezger, *Applied Rheology with Joe Flow on Rheology Road*, Anton Paar GmbH, Germany, 2014.
45 M. M. Cross, *J. Colloid Sci.*, 1965, **20**, 417–437.

46 J. Sunder and A. Goettfert, *ANTEC 2001 Proceedings*, Dallas, 2001.
47 R. S. Lenk, in *Polymer Rheology*, Springer Netherlands, Dordrecht, 1978, pp. 75–85.
48 E. J. Hearn, *An Introduction to the Mechanics of Elastic and Plastic Deformation of Solids and Structural Materials*, Butterworth-Heinemann, Oxford, 1997.
49 B. R. Hunt, R. L. Lipsman and J. M. Rosenberg, *A Guide to MATLAB: for Beginners and Experienced Users*, Cambridge University Press, 2014.
50 F. E. Grubbs, *Technometrics*, 1969, **11**, 1–21.
51 G. Ashiotis, A. Deschildre, Z. Nawaz, J. P. Wright, D. Karkoulis, F. E. Picca and J. Kieffer, *J. Appl. Crystallogr.*, 2015, **48**, 510–519.
52 W. Gindl, K. J. Martinschitz, P. Boesecke and J. Keckes, *Biomacromolecules*, 2006, **7**, 3146–3150.
53 X. Liu, J. Pang, X. Zhang, Y. Wu and R. Sun, *Cellulose*, 2013, **20**, 1391–1399.
54 L. K. J. Hauru, *Doctor of Science in Technology Doctoral Thesis*, Aalto University, 2017.
55 V. Bertola, B. Meulenbroek, C. Wagner, C. Storm, A. Morozov, W. van Saarloos and D. Bonn, *Phys. Rev. Lett.*, 2003, **90**, 114502.
56 G. Schramm, *A Practical Approach to Rheology and Rheometry*, Thermo Electron GmbH, Germany, 2004.
57 A. D. French, *Cellulose*, 2013, **21**, 885–896.
58 X. L. Xia, Y. B. Yao, X. J. Zhu, K. S. Mukuze, C. S. Wang, Y. M. Zhang and H. P. Wang, *Mater. Res. Innovations*, 2014, **18**, S2-874–S2-878.
59 S. Elsayed, M. Hummel, D. Sawada, C. Guizani, M. Rissanen and H. Sixta, *Cellulose*, 2020, **28**, 533–547.
60 B. Zhang, J. Azuma and H. Uyama, *RSC Adv.*, 2015, **5**, 2900–2907.
61 H. Qi, C. Chang and L. Zhang, *Green Chem.*, 2009, **11**, 177–184.